A modell for fragmentation of hard metallic targets due to projectile perforation

GUNNAR WIJK

FOI is an assignment-based authority under the Ministry of Defence. The core activities are research, method and technology development, as well as studies for the use of defence and security. The organization employs around 1350 people of whom around 950 are researchers. This makes FOI the largest research institute in Sweden. FOI provides its customers with leading expertise in a large number of fields such as security-policy studies and analyses in defence and security, assessment of different types of threats, systems for control and management of crises, protection against and management of hazardous substances, IT-security an the potential of new sensors.

FOI
Defence Research Agency
Weapons and Protection
SE-147 25 Tumba

Phone: +46 8 555 030 00
Fax: +46 8 555 031 00

www.foi.se

FOI-R-- 1733 --SE **Weapons and Protection** October 2005
ISSN 1650-1942 Scientific report

A model for fragmentation of hard metallic targets due to projectile perforation

FOI-R--1733--SE
ISSN 1650-1942

Weapons and Protection
Scientific report

October 2005

Issuing organization	Report number, ISRN	Report type
FOI – Swedish Defence Research Agency Weapons and Protection SE-147 25 Tumba	FOI-R--1733--SE	Scientific report
	Research area code 5. Strike and protection	
	Month year October 2005	**Project no.** E2007
	Sub area code 51 Weapons and Protection	
	Sub area code 2	

Author/s (editor/s)	Project manager
Gunnar Wijk	Gunnar Wijk
	Approved by
	Sponsoring agency
	Scientifically and technically responsible

Report title

A model for fragmentation of hard metallic targets due to projectile perforation

Abstract (not more than 200 words)

When a projectile perforates a hard metallic target it will emerge with a bundle of fragments from the target material. A model is suggested for the production of these fragments, which gives the total mass as well as the distribution of fragment masses, velocities and directions of motion. The intended application of the model is in computer programs for assessment of effects and vulnerability of complex targets such as tanks, fighters and naval ships. For this purpose rather simple physical models, such as the one suggested in this report, are to prefer instead of mostly empirical models. The suggested model involves two different fragment groups. One group consists of larger (spalling) fragments with velocities associated with the particle velocities from elastic wave reflection at the rear target surface. The other group has smaller total mass and consists of smaller but faster-moving fragments that are accelerated through contact with the residual projectile. The mass ratio between these two groups is a crucial parameter in the model and must be determined from experimental results. In reality the smaller but faster-moving fragments overtake the larger spalling fragments, but this complication is neglected in the model.

Keywords

Fragments, projectile, perforation, model

Further bibliographic information	Language English
ISSN 1650-1942	**Pages** 22 p.
	Price acc. to pricelist

Utgivare	Rapportnummer, ISRN	Klassificering
FOI - Totalförsvarets Forskningsinstitut -	FOI-R--1733--SE	Vetenskaplig rapport
Vapen och skydd	**Forskningsområde**	
147 25 Tumba	5. Bekämpning och skydd	
	Månad, år	**Projektnummer**
	Oktober 2005	E2007
	Delområde	
	51 VVS med styrda vapen	
	Delområde 2	

Författare/redaktör	Projektledare
Gunnar Wijk	Gunnar Wijk
	Godkänd av
	Uppdragsgivare/kundbeteckning
	Tekniskt och/eller vetenskapligt ansvarig

Rapportens titel (i översättning)

Modell för splitterproduktion vid projektilgenomträngning av hårda metalliska materiall

Sammanfattning (högst 200 ord)

När en projektil perforerar ett mål av hård metall kommer den ut med en svärm av splitter från målet. En modell föreslås för produktionen av dessa splitter. Modellen omfattar såväl den totala massan av splitter som fördelningarna av splittermassor, splitterhastigheter och rörelseriktningar. Den avsedda tillämpningen är i program för värdering av verkan och sårbarhet för komplexa mål som stridsvagnar,, stridsflygplan och örlogsfartyg. Till detta ändamål är förhållandevis enkla fysikaliska modeller, som den som föreslås i rapporten, att föredraga framför huvudsakligen empiriska modeller. I den föreslagna modellen är splittren av två olika slag. En grupp består av stora fragment som produceras i via utstötning samband med reflektion av elastiska vågor från målets baksida, varför splitterhastigheterra följaktligen är begränsade. Den andra gruppen har mindre totalmassa och består av mindre splitter som accelererats genom direktkontakt med projektilen och därmed (normalt) har mycket högre hastigheter än i den första gruppen. Massförhållandet mellan grupperna är en väsentlig modellparameter som måste bestämmas experimentellt. I verkligheten hinner de mindre men fortare flygande splittren i kapp de långsammare utstötningssplittren, men denna komplikation försummas i modellen.

Nyckelord

Splitter, projektil, genomträngning, modell

Övriga bibliografiska uppgifter	Språk Engelska
ISSN 1650-1942	**Antal sidor:** 22 s.
Distribution enligt missiv	**Pris: Enligt prislista**

Nomenclature

B non-dimensional parameter in mass distribution
c_T elastic wave velocity in target material, m/s
D_T hole diameter in target material, m
D_{exit} maximum exit hole diameter in target material, m
d_P initial projectile diameter, m
E_T elastic modulus of target material, Pa
h target thickness, m
h^* transition thickness between penetration and perforation, m
$h^{(*)}$ thickness of fragmented plug, m
j number of layer of fragments
L projectile length, m
M accumulated mass of fragments, kg
m residual projectile mass, kg
m_P initial projectile mass, kg
m_T total mass of fragments from rear target surface, kg
m_i mass of i^{th} fragment from rear target surface, kg
N total number of fragments
N_S number of fragments from rear target surface layer
N_{NS} number of fragments from rear target layer next to surface layer
p_r spherical pressure wave amplitude, Pa
r radial distance, m
n accumulated number of fragments
u target fragment velocity, m/s
Y_T uniaxial yield strength of target material, Pa
v instantaneous projectile velocity, m/s
v^* projectile velocity at penetration depth $h-h^{(*)}$, m/s
v_P projectile impact velocity, m/s
v_{exit} exit velocity for residual projectile, m/s
v_T characteristic target velocity parameter, m/s
W projectile impact energy, J
W_p minimum target perforation energy, J
Y_T uniaxial yield strength for target material, Pa
Y_P uniaxial yield strength for projectile material, Pa
α fraction of target fragments that is produced by spalling
β_T non-dimensional target penetration resistance parameter
δ_i side length of i^{th} (cubic) fragment from rear target surface, m
δ_S average thickness of surface layer of fragments, m
λ non-dimensional parameter in mass distribution
ρ_T target density, kg/m^3
ρ_P projectile density, kg/m^3
ψ_T non-dimensional hole size parameter
Ψ maximum angle for direction of motion for a fragment
ϑ angle for direction of motion for a fragment
Θ half apex angle for truncated cone that becomes fragments
θ half apex angle of conical- or ogive-nosed projectile

Introduction

A model for rigid projectile penetration and perforation of hard metallic targets is suggested in [1]. When a projectile penetrates a target, then the material immediately in front of it is moved so that it finally becomes displaced in the lateral direction. During an

initial phase, when the penetration depth is not several times larger than the projectile diameter, the target resistance increases to $\beta_T Y_T$, where Y_T is the yield strength for the target material [2]. A representative value for the penetration coefficient is β_T=5.

A model for eroding projectile penetration is suggested in [3, 4] and is closely related to the model for rigid projectile penetration in [1] with respect to the behaviour of the target material. In the appendix to the present report the penetration model in [3, 4] for eroding projectiles is extended to account for perforation in a similar manner as for rigid projectiles in [1, 2].

At a certain penetration depth the penetration phase stops and the perforation phase starts [1 - 4], whereby the remaining part of an eroding projectile is assumed to be rigid. The target material m_T in front of the projectile is assumed to be instantaneously crushed to fragments, which requires certain energy and a corresponding reduction of the projectile velocity from the value that it has been reduced to during the penetration phase. Thereupon the fragments in front of the projectile are accelerated, causing further reduction of the projectile velocity to the final exit velocity v_{exit}. If friction is negligible and the exit velocity vanishes, then the kinetic energy of the fragments also vanishes and the kinetic impact energy W is equal to the minimum perforation energy W_p. If friction is not negligible, then the fragments will have higher velocity than v_{exit}, which may vanish if W is not sufficiently much higher than W_p [2]. The models in [1 - 4] and the Appendix yield the energy W_p and the mass m_T as functions of the projectile and target parameters.

In the present report a model for the distribution of masses, velocities and directions of motion for the fragments, which is based on numerical and experimental results in [5] and experimental results in [6], and the corresponding exit velocity for the projectile is suggested. Such extension of the model for projectile penetration and perforation is necessary for the intended application.

In connection with this work two reviews of the literature concerning production of fragments due to projectile perforation have been conducted, one with respect to models and simulation and the other with respect to experiments [7, 8]. It should be emphasised that none of these suggests a model for the whole process of projectile penetration, perforation and fragment production in a coherent manner.

Model for the total mass of fragments

With the models in [1 - 4] the hole diameter D_T is equal to the projectile diameter d_P if the projectile is rigid and is greater if it is eroding. In the latter case D_T depends on the instantaneous projectile velocity v and a characteristic velocity v_T for the target material so that

$$D_T = d_P \frac{v}{v_T} \tag{1}$$

with

$$v_T = \psi_T \sqrt{\frac{\beta_T Y_T}{\rho_T}}, \tag{2}$$

where ρ_T is the target density and ψ_T is an experimentally determined coefficient that differs marginally from one target material to another. *Undisturbed* eroding projectile penetration does not only require that $v>v_T$, but that v is higher than a velocity $v_{\lim}>v_T$ so that there is room for the eroded projectile material in the hole [4]. For $v<v_{\lim}$ there is *disturbed* eroding projectile penetration. The mathematical relations for $v>v_{\lim}$ and $v<v_{\lim}$ are continuously connected for $v=v_{\lim}$.

When the front end of a projectile reaches the transition distance h^* from the rear surface of a hard metallic target, then the remaining material in front of the projectile is assumed to be instantaneously fragmented, which requires the additional energy W_p^* as in the Appendix. The distance h^* is somewhat larger than D_T. When $h<h^*$ perforation occurs without a preceeding penetration phase. The mass of fragments is assumed to be given by the cylindrical plug in front of the projectile when perforation starts

$$m_T \approx \frac{\pi}{4} D_T^2 \, h^{(*)} \, \rho_T \,, \tag{3}$$

where $h^{(*)} = h$ for $h<h^*$ and $h^{(*)} = h^*$ for $h>h^*$.

In reality, for $h>h^*$ fragments originate from a plug that is shaped roughly as a truncated cone with a larger diameter D_{exit} at the surface and with a smaller height than h^*. It is suggested that the conical plug is defined by having the same mass, the same smaller (inner) end diameter as the cylindrical plug and, consequently, also a smaller height (length). Somewhat arbitrarily, the height of the conical plug is assumed to equal the diameter of the smaller (inner) end, from which it follows that

$$D_{exit} = \sqrt{3 D_T \, h^* + \frac{D_T^2}{4}} - \frac{D_T}{2} \,. \tag{4}$$

For a representative value of the transition thickness h^* as defined in [1, 2], namely $h^* \approx 1.4 \, D_T$, Eq. (3) yields $D_{exit} \approx 1.6 D_T$. The half apex angle Θ for the truncated cone plug is given by

$$\Theta = \arctan\left(\frac{D_{exit} - D_T}{2 \, D_T} \right). \tag{5}$$

For $h^* \approx 1.4 \, D_T$ Eq. (5) yields $\Theta \approx 17^{\circ}$. Accordingly it is assumed that the angle Θ is independent of the projectile nose shape.

Model for mass distribution of fragments

A model concerning production of target fragments in connection with projectile perforation is described in [5], where [5, Figure 5] shows the front end of an eroding projectile, which is close to the rear target surface. A mass m_T of fragments is produced in front of the projectile. A similar picture but for a rigid projectile is shown in Figure 1.

An important feature of the model represented by Figure 1 is that the largest fragments are produced from the rear surface of the target and that the fragment size decreases inwards. It should be emphasised that the model in [5] is tacitly understood to be used for thick targets. The difference between thick and thin targets is defined in [1, 2] for rigid projectiles and in the Appendix for eroding projectiles. The target is thick for $h>h^*$ and thin for $h<h^*$.

A picture of the residual projectile after perforation, surrounded by accelerated *small target fragments* and projectile fragments at times 100, 125, 150, 175, 200 and 225 μs is shown in [5, Figure 14]. A reproduction of the two of last situations is shown in Figure 2. It is stated in [5] that a *significant fraction of the target mass loss corresponds to the ringlike segment detached from the rear surface of the target. The formation of the ringlike segment is out of the scope of the model at present*. For the intended application of the model it is believed that all fragments must be accounted for. Consequently the

general features in Figures 1 and 2 are suggested to be extended to cover all fragments but in simpler mathematical form than those in [5].

A model for the distribution of target fragment masses is suggested in [6]. The accumulated mass $M(n)$ of the n largest fragments is

$$M(n)=m_T\left\{1-\exp\left(-B\,n^{\lambda}\right)\right\} \tag{6}$$

where B and λ are non-dimensional, empirical parameters. Experimental evaluation of two cases corresponding to projectile perforation of target plates yield B=0.1103, λ=0.6357 and B=0.1010, λ=0.5087. Without experimental results, from which B and λ can be determined, it is suggested here that

$$B=0.10 \tag{7}$$

and

$$\lambda=0.50 \tag{8}$$

should be used.

A computer program for assessment of effects and vulnerability for complex targets can be based on the Monte Carlo method for calculation of probabilities for events. Instead of using the fixed values in Eqs. (7) and (8) these parameters may be changed, from one Monte Carlo cycle to another, via random numbers and appropriately chosen distributions with average values given by Eqs. (7) and (8). In this manner realistic scatter is introduced in the computer program. Similar use of the Monte Carlo method is also suggested for several other situations described below.

When $B<<1$, as in Eq. (7), the mass of the largest fragment is

$$m_1 \approx B\,m_T\,. \tag{9}$$

Similarly the mass of fragment number n is

$$m_n \approx m_T\,B\,\lambda\,n^{\lambda-1}\exp\left(-B\,n^{\lambda}\right). \tag{10}$$

Model for fragments trajectories

All fragments are approximated by cubes. Thus the side of the largest fragment is

$$\delta_1 \approx \sqrt[3]{\frac{m_1}{\rho_T}}\,. \tag{11}$$

If all fragments from the surface are temporarily assumed to have the same size, then the number of surface fragments is

$$N_{S,\min} \approx \frac{\pi\,D_{exit}^2}{4\,\delta_1^2}\,. \tag{12}$$

The mass of the fragment with number $n=N_{S,\min}$ is given by

$$m_{N_{S,\min}} \approx m_T\,B\,\lambda\,N_{S,\min}^{\lambda-1}\,\exp\left(-B\,N_{S,\min}^{\lambda}\right). \tag{13}$$

The corresponding side of this fragment is

$$\delta_{N_{S,\min}} \approx \sqrt[3]{\frac{m_{N_{S,\min}}}{\rho_T}} . \tag{14}$$

If instead all fragments from the surface are temporarily assumed to have the same size as that with number $n=N_{S,\min}$, then the number of surface fragments is

$$N_{S,\max} \approx \frac{\pi D_{exit}^2}{4\delta_{N_{S,\min}}^2} . \tag{15}$$

The model for the number of fragments from the surface is suggested to be the integer closest to the geometric average of the numbers $N_{S,\min}$ and $N_{S,\max}$ so that

$$N_S \approx \sqrt{N_{S,\max} N_{S,\min}} . \tag{16}$$

The N_S fragments are distributed within the cone with the apex angle 2Θ in Figure 1. This cone defines a spherical sector, which is part of a sphere with unit radius around the apex. The spherical sector area is $4\pi\sin^2(\Theta/2)$. This area is divided into N_S parts, and the surface fragment trajectories are assumed to pass through mid-points of these parts. The parts are approximately trapezoidal except for the innermost ones, which are approximately triangular, as shown in Figure 2. The mid-points are simply defined by the cross-points for the diagonals from the corners of the trapetzoids and by the cross-points for the bisectors of the triangles.

Along the periphery of the spherical sector with the area $4\pi\sin^2(\Theta/2)$ there are $N_{S,1}$ trapezoids, each with the area $4\pi\sin^2(\Theta/2)/N_S$. Thus the average base length of these trapetzoids is $2\pi\sin(\Theta)/N_{S,1}$. Since approximately the trapetziods are sides of cubes the height is (assumed to be) equal to the base length. In practice the angle Θ is rather small so that $\sin(\Theta)\approx\Theta$. Thus the height of the periphery fragments is $\pi D_{exit}/N_{S,1}$, as shown in Figure 1, and the area of a peripheral trapetzoid is $\{2\pi\sin(\Theta)/N_{S,1}\}^2\{1-\tan(\pi/N_{S,1}\}$. The two expressions for the area determine the number $N_{S,1}$ as the numerical solution to

$$N_{S,1}^2 = \pi N_S \frac{\sin^2(\Theta)}{\sin^2\left(\frac{\Theta}{2}\right)}\left\{1-\tan\left(\frac{\pi}{N_{S,1}}\right)\right\} . \tag{17}$$

The solution of Eq. (17) is generally not an integer, which means that the closest integer value should be chosen. The spherical sector area inside these $N_{S,1}$ trapetzoids defines a smaller apex angle $2\Theta_1$, which is given by

$$\Theta_1 = 2\arcsin\left\{\sin\left(\frac{\Theta}{2}\right)\sqrt{1-\frac{N_{S,1}}{N_S}}\right\} . \tag{18}$$

Accordingly the number $N_{S,2}$ of fragment trajectories that are closest to the periphery of this spherical sector with the circumference $2\pi\sin(\Theta_1)$ is obtained as the closest integer to the solution to

$$N_{S,2}^2 = \pi N_S \frac{\sin^2(\Theta)}{\sin^2\left(\frac{\Theta_1}{2}\right)}\left\{1-\tan\left(\frac{\pi}{N_{S,2}}\right)\right\}. \quad (19)$$

Simliarly

$$\Theta_2 = 2\arcsin\left\{\sin\left(\frac{\Theta}{2}\right)\sqrt{1-\frac{N_{S,1}+N_{S,2}}{N_S}}\right\}. \quad (20)$$

and so on until $N_{S,1}+N_{S,2}+\ldots \approx N_S$ is obtained. In this manner the mid-points of all the surface fragment trajectories are defined, except for arbitrary rotations of the rings of fragment directions around the axis of the cone. These rotation angles should be determined via random numbers for every Monte Carlo cycle.

Random numbers should also be used to determine which of the N_S trajectories each of the N_S surface fragments will follow. Accordingly the largest surface fragment will generally go in different directions from one Monte Carlo cycle to another.

In Figure 2 the next few layers of fragments contain the same number of fragments as the surface layer. This will generally not be the case when the next layer of fragments is treated in analogy with the surface layer in Eqs. (11) – (20) since the number N_{NS} of fragments in this next layer will normally differ from the number N_S in the surface layer. In analogy with Eq. (11) the calculation starts with

$$\delta_{N_S+1} \approx \sqrt[3]{\frac{m_{N_S+1}}{\rho_T}}. \quad (21)$$

In analogy with Eq. (16) the average thickness of the surface layer is (assumed to be) given by

$$\delta_S = \sqrt{\delta_1\, \delta_{N_{S,\min}}}. \quad (22)$$

Accordingly the outer diameter of the next layer of fragments is assumed to be given by D_{exit} - $2\delta_S\tan(\Theta)$. In analogy with Eq. (12) the minimum number of fragments from the next layer is given by

$$N_{NS,\min} \approx \frac{\pi\left\{D_{exit}-2\,\delta_S\tan(\Theta)\right\}^2}{4\,\delta_{N_S+1}^2}, \quad (23)$$

whereupon continued calculations follow the scheme in Eq. (13) – (20). Subsequent layers of fragments are treated in the same manner.

In Figure 2 the trajectories for all fragments cross the axis at about the same point along the axis except the outermost ones, which cross the axis somewhat closer to the rear target surface. However, for simplicity it is assumed that these also cross the axis at the same point as the others, which is at the distance z from the rear target surface. This point and the mid-points of the trapetzoids and triangles mentioned above define the trajectories for all fragments. Accordingly the outermost fragments follow trajectories along a conical surface with the apex angle Ψ as shown in Figure 1.

It is likely that Ψ should depend on the shape of the nose of the projectile so that a sharp-nosed projectile corresponds to larger Ψ than a blunt-nosed projectile. Maximum bluntness corresponds to a flat-nosed projectile, which may be regardad as the limit

$\theta=\pi/2$ of a conical-nosed projectile. However, in practice projectiles are never flat-nosed but have ogival nose shape, which is characterised by a half apex angle θ and a radius R for the ogival surface. The length of the nose is given by $R\sin(\theta)$ and $\sqrt{\{2R-d/2\}d/2}$. Equality between these two expressions defines the relations $R=R(\theta,d)$ and $\theta=\theta(R,d)$. When the apex angle approaches the limit $\theta=\pi/2$, then the projectile nose becomes hemispherical. The nose shape of an eroding projectiles is not known, but in [5, Figure 13] the hole bottom in front of an initially flat-nosed projectile is approximately hemispherical already when the penetration depth is about $D_T/2$. Until there are experimental results that call for some other model it is suggested that the trajectory apex angle Ψ is determined from the projectile apex angle θ via the simple linear relation

$$\Psi=\frac{\pi}{2}-\frac{2\theta}{3}\ . \tag{24}$$

Thus a spherical-(or flat-)nosed projectile corresponds to $\Psi\approx\pi/6=30^o$, whereas $\theta\approx\pi/4$ corresponds to $\Psi\approx\pi/3=60^o$.

Accordingly the apex point in Figure 1 for the fragment trajectories is (assumed to be) located at the depth

$$z=\left\{\frac{D_{exit}}{2}-\frac{\pi\sin(\Theta)}{N_{S,1}}\right\}\cot(\Psi). \tag{25}$$

Model for the velocities of fragments

When a projectile penetrates a target elastic-plastic waves continuously emerge from the front end of the projectile. The corresponding dynamic stress-and-strain field in the target cannot be obtained by use of analytical methods. However, the radial pressure wave amplitude at radial distance r and time t around a spherical cavity with diameter D_T in an infinitely large medium of solid material, due to internal pressure that is high enough to cause plastic flow in the cavity wall, namely at $r=D_T/2$, should be similar to the corresponding pressure wave in a fluid [9]

$$p_r(r,t)=\frac{D_T}{2r}\,p\left(\frac{D_T}{2},t-\frac{2r-D_T}{2c_T}\right), \tag{26}$$

where c_T is the (relevant) wave velocity. In the present connection Eq. (26) is assumed to yield a sufficiently good approximation of the real elastic pressure wave in front of a penetrating projectile with the one-dimensional elastic wave velocity

$$c_T=\sqrt{\frac{E_T}{\rho_T}}\ . \tag{27}$$

Here E_T is the elastic modulus for the target material. The pressure at the radius $D_T/2$ is assumed to be given by the penetration resistance in [1, 2, 4]. Accordingly

$$p_r(r,t)=\frac{\beta_T\,Y_T\,D_T}{2r}\,H\left(t-\frac{2r-D_T}{2c_T}\right), \tag{28}$$

where $H(t)=1$ for $t>0$ and $H(t)=0$ for $t<0$. When this pressure wave reaches the rear target surface then two waves are reflected, namely a tensile (or negative pressure) wave and a shear wave. The relative amount of tension and shear varies with the angle of

incidence for the pressure wave against the rear target surface (at the point straight ahead of the projectile, where the incidence angle is 90^o, there is only tension).

Reflection of the incident pressure wave in Eq. (28) at the rear target surface may cause spalling (multiple fracturing) when the radial distance r to the rear target surface becomes so small that the incident pressure at the rear surface equals Y_T. Strictly this is not a sufficient criterion since the local specific compression and kinetic energy must be high enough to provide the surface energy corresponding to crack creation [10]. However, at the point on the rear target surface that is straight ahead of the projectile this occurs (with delay since the wave velocity c_T is finite) for the distance h^* between the bottom of the hole and the rear target surface. Thereby the radial distance is $r = h^* + D_T / 2$ in Eq. (28), which yields

$$h^* = D_T \frac{\beta_T - 1}{2}. \tag{29}$$

For other points on the rear target surface the incident pressure equals Y_T for smaller distances between the bottom of the hole and the rear target surface. Consequently an empirical relation for the distance h^*, at which spalling occurs in connection with projectile perforation of a target, should be smaller than the "physical" result in Eq. (29). For the empirical models suggested in [1, 2] and Eqs. (A3), (A5) and (A10) in the Appendix the denominator in Eq. (29) is π instead of 2.

For the one-dimensional case the maximum velocity of spalling fragments from the rear surface of the target is

$$u_{S,\max} \approx \frac{2 c_T Y_T}{E_T}. \tag{30}$$

Fragments ejected at small angles to the projectile trajectory should travel with velocities close to $u_{S,max}$, whereas fragments that are ejected at larger angles should be slower. For hard steel targets with $c_T \approx 5$ km/s, $E_T \approx 210$ GPa and $Y_T \approx 1$ GPa Eq. (30) yields $u_{S,max} \approx 50$ m/s. This result agrees qualitatively, and probably also quantitatively, with the visual impression from experimental results in [11, Chapter 5, Figures 71 - 74], where the velocities of the larger fragments are many times smaller than the exit velocity of the projectile, which is closely accompanied by a cloud of small fragments. Thus it seems to be necessary to consider the total fragment mass mass m_T to consist of a larger part $m_{T,S}$ with large and slow-moving fragments and a smaller part $m_{T,F}$ with small fast-moving fragments. It is then necessary to introduce a model for the ratio

$$\alpha = \frac{m_{T,S}}{m_T} = 1 - \frac{m_{T,F}}{m_T} \tag{31}$$

between the total mass of the spalling fragments and the total mass of all secondary fragments. According to Eqs. (6) and (31) the number i of the largest fast-moving fragment is then given by

$$i = \left\{ -\frac{1}{B} \log(1 - \alpha) \right\}^{\frac{1}{\lambda}}. \tag{32}$$

According to Figure 2 the velocities of fragments decrease with increasing angle ϑ to the direction of motion of the residual projectile, the mass of which is m (for a rigid

projectile m is equal to the initial mass m_P). The velocity for the fastest and innermost fragment is about equal to the projectile exit velocity v_{exit}. The velocity for the fastest and outermost fragment, for which $\vartheta \approx \Psi$, does not vanish but is about half of the velocity for the innermost fragment. Accordingly an assumption for how the velocity of the fastest fragments should vary with the direction is given by

$$u_{F,exit,1} = v_{exit} \cos\left(\frac{\pi \vartheta}{3\Psi}\right). \tag{33}$$

In Figure 2 fragments from deeper layers have smaller velocities. If the velocity of a foremost fragment is $u_{F,exit,1}$ and the velocity of the following fragment is $u_{F,exit,2}$, then measurements of positions of fragments in Figure 2 show that $u_{F,exit,2}/u_{F,exit,1} \approx 0.8$ yields a reasonable description for $0 < \vartheta \leq \Psi$. Differences between real starting points are negligible when the velocity ratio is evaluated with such rough accuracy. The velocity ratios for subsequent pairs of layers increase so that $u_{F,exit,3}/u_{F,exit,2} \approx 0.9$, $u_{F,exit,4}/u_{F,exit,3} \approx 0.93$, $u_{F,exit,5}/u_{F,exit,4} \approx 0.95$ and so on. These ratios are evaluated from a rather arbitrarily chosen, common and simultaneous starting point for all the fragments in Figure 2. The second decimal number in these ratios is quite uncertain but it indicates the magnitude of the effect in a reasonable way. A simple mathematical model for these velocity ratios between subsequent pairs of layers is given by

$$\frac{u_{F,exit,j+1}}{u_{F,exit,j}} \approx 1 - \frac{0.2}{j}, \tag{34}$$

and is assumed to remain reasonable for greater values of j.

For simplicity the model for the angle-and-layer dependence of velocities of small fast-moving fragments in Eqs. (33) and (34) is also assumed to hold for large slow-moving fragments so that

$$u_{S,exit,1} = u_{S,\max} \cos\left(\frac{\pi \vartheta}{3\Psi}\right). \tag{35}$$

and

$$\frac{u_{S,exit,j+1}}{u_{S,exit,j}} \approx 1 - \frac{0.2}{j}. \tag{36}$$

The model represented by Eqs. (33) - (36) corresponds to the exit kinetic energy

$$W_{exit} = \frac{1}{2} m v_{exit}^2 + \frac{1}{2} \sum_{i=n}^{\infty} m_i u_n^2. \tag{37}$$

In order to determine v_{exit} this energy is also assumed to be given by

$$W_{exit} = W - W_p. \tag{38}$$

In reality there should be some additional energy loss due to friction and deformation during the acceleration of the small fast-moving fragments. Furthermore, the kinetic energy for the large slow-moving fragments should be part of the energy W_p^* in the

Appendix. However, the large slow-moving fragments are initially in front of the small slow-moving fragments. Thus there will necessarily be a multitude of interactions, which correspond to change of velocities and directions of motion for the fragments involved, before all faster-moving fragments are in front of all slower-moving fragments. Such complications are deliberately neglected in the model above as well as in [5].

It should be emphasized that the fragments in [5, Figure 14] and Figure 2 are not only from the target but also from the (eroding) projectile.

Comparison with experimental results

In the experiments in [5] the projectile diameter and initial length are d_P=20 mm and L=120 mm, respectively. The projectile material is "tungsten sintered alloy" with density ρ_P=17.13 g/cm^3 and Brinell hardness BHN 430, which is assumed to corresponds to the yield strength Y_P≈BHN/300≈1.4 GPa. The impact velocity is v_P≈1.70 km/s. The target material is steel with density ρ_P=7.85 g/cm^3 and Brinell hardness BHN 330, which is assumed to correspond to the yield strength Y_T≈BHN/300≈1.1 GPa.

Experimental results for two target thicknesses are reported in [5, Table 2]. For h=40 mm the residual projectile length is about 83 mm and the corresponding velocity is v_{exit}≈1.58 km/s. The two tests resulted in the hole diameter D_T=49.8 and 42.4 mm, the corresponding target mass loss m_T=674 and 524 g and the correponding projectile mass loss 197.3 and 201.1 g. For h=70 mm the residual projectile length is about 59 mm and the corresponding velocity is v_{exit}≈1.50 km/s. The two tests resulted in the hole diameter D_T=41.0 and 42.4 mm, the corresponding target the mass loss m_T=685 and 597 g and the correponding projectile mass loss 321.1 and 329.1 g.

According to the model in [4] a flat-nosed projectile, which impacts a semi-infinite target, should be eroded already from the impact time if $Y_P<3Y_T$. For the materials in [5] this criterion is well satisfied, in agreement with the picture in [5, Figure 13]. Furthermore, the relative reduction of projectile length should be much larger than the relative reduction of projectile velocity, which also agrees with the findings in [5]. The projectile mass loss for h=70 mm is about 1.6 times larger than for h=40 mm. Thus the projectile mass loss seems to be approximately proportional to the target thickness, which indicates that projectile erosion continues during most of the penetration-and-perforation, as suggested at the end of the Appendix.

Half of the hole diameter D_T above is called *crater radius* in [5, Table 2]. More specifically, it is the *measured minimal crater radius* and it is assumed *that the material from the wider parts of the crater near the front and rear sides of the target belongs to the fractured zone, and has been ejected*. The lateral dimensions of the targets are not specified in [5], but the numerical calculations are for targets with the initial external diameter about 93 mm or roughly only twice the hole diameter D_T, as measured with a ruler in [5, Figure 13]. After penetration the final external diameter is measured to be 100±1 mm. According to [2, 4] the penetration resistance for such small targets is significantly smaller than for infinitely large targets. If finite targets shall be reasonably representative for infinitlely large targets, then the initial external diameter must be at least, say, 15 times greater than the final hole diamater D_T. When this requirement is not satisfied, then the penetration resistance coefficient β_T or the characteristic velocity parameter ψ_T or both are significantly smaller than for an infinitely large target.

The projectile velocity reduction in the experiments in [5] is small enough to be neglected when the velocity parameter ψ_T in Eq. (2) is evaluated. A represenative value for the measured hole diameters above is D_T=44 mm. With this value Eqs. (1) and (2), v=1.7 km/s and β_T=5 yield v_T≈0.77 km/s and ψ_T≈0.91. This value is significantly smaller than the corresponding values for tungsten alloy projectiles and steel targets in [4], namely ψ_T≈1.1.

There is no specification of *the wider parts of the crater near the front and rear sides of the target* [5]. If the crater is assumed to be cylindrical with the diameter D_T=44 mm,

then the volume of the hole in the target with thickness h=70 mm is about 106 cm^3 and corresponds to the mass about 830 g, which is significantly greater than the measured mass losses m_T. However, the external volume increase of the target that is measured in [5, Figure 13] is $7.0\pi(10.0^2\text{-}9.3^2)/4\approx74$ cm^3. Accordingly, the target volume and mass loss must be at least 106-74≈32 cm^3 and about 250 g. The average mass loss for the four tests above is 620 g or about 2.5 times larger. Thus *the wider parts of the crater near the front and rear sides of the target* are significantly larger than D_T, as they are stated to be.

Since the velocity v_{exit}≈1.6 km/s is so close to the impact velocity v_P≈1.7 km/s it is reasonable to assume that penetration-and-perforation correspond to an initial hole with the constant diameter 44 mm. Thus Eqs. (A5) and (A8), $D_T^* = 44$ mm and β_T=5 yield $h^* \approx 56$ mm and m_T≈668 g. The latter is only slightly larger than the experimental result for the average target mass loss above. It is natural to expect the rear side crater in the target to be significantly larger than the front side crater, especially for a flat-nosed projectile as in [5, Figure 13].

In the discussion in connection with Eqs. (3) - (5) it is suggested that the rear side crater has the shape of a truncated cone with the height equal to the hole diameter. The actual hole diameter D_T≈44 mm is almost equal to the smaller target thickness in [5]. If the rear side crater is significantly larger than the front side crater, then the target mass loss m_T should be about the same for the two actual thicknesses, which is in agreement with the experimental results. For the thinner target fragment ejection starts almost immediately after impact, whereas the projectile has to penetrate about h-D_T≈26 mm of the thicker target before fragment ejection starts.

As already mentiond just before Eq. (6) it is stated in [5] that a *significant fraction of the target mass loss corresponds to the ringlike segment detached from the rear surface of the target. T*he corresponding fragments are not accounted for in [5]. Unfortunately, this *significant fraction of the target mass loss* is the part $m_{T,S}$ that is represented by the model in Eq. (5). If it is assumed that $m_{T,S}$≈600 g and $m_{T,F}$≈60 g, with which Eq. (29) yields α≈0.91, then Eqs. (5) - (7) and (10) yield m_1≈60 g, δ_1≈19 mm and m_2≈24 g. If the velocity of the largest fragment is $u_{S,max}$≈50 m/s, then the kinetic energy is about 75 J.

Experimental results for the distribution of *small target fragment* masses for h=40 and 70 mm are given in [5, Figures 10 and 11]. The results are rather similar so only the case h=70 mm is examined below. The results in [5, Figure 11] are shown in Table 1. In both tests the reported mass of the largest fragment is m_1=1.9+ g, where the + means that the real mass is somewhere in the interval from 1.9 to 2.0 g. The total mass $m_{T,F}$ is not specified. From Exp. 607 there are altogether 54 reported fragments with the accumulated mass somewhere between M(54)=30.7 and 84.7 g. The largest contribution to the minimum value comes from the group with 7 fragments with mass 0.8+ g, and the second largest contribution comes from the the group with 3 fragments with mass 1.0+ g. With these numbers in mind it seems quite safe to assume that the unknown contribution from the group with fragments with mass m_{20}=0.0+ g should be less than a few grams. This contribution is negligible in comparison with the uncertainty in the value M(54) above. Accordingly the total mass of small fast-moving fragments is assumed to be just slightly larger than the average of the minimum and maximum values for M(54), namely $m_{T,F}$=60 g, in agreement with the assumption above.

For Exp. 530 with m_T≈685 g the accumulated mass for 81 target fragments is somewhere between M(81)=50.1 and 131.1 g. The largest contribution to the minimum value comes from the group with 5 fragments with mass 0.8+ g, and the second largest contribution comes from the the group with 5 fragments with mass 0.7+ g. The average of the minimum and maximum values for M(81), namely $m_{T,F}$≈90 g, is somewhat larger in comparison with the total fragment mass m_T than in the previously considered experiment, but the *significant fraction of target mass loss*, namely α≈0.87, is similar.

The velocity of the fastest fragments in Figure 2 is v_{exit}≈1.5 km/s. If this is also the velocity of the largest fragment, then the corresponding kinetic energy is about 2.1 kJ or almost 30 times higher than for the most energetic spalling fragments above.

If the projectile mass and volume loss for the target thickness h=70 mm in [5, Table 2], namely about 325 g and 19 cm^3, is evenly distributed along the surface of a hole with diameter D_T=44 mm, then the thickness of the layer of eroded projectile material is about 2.0 mm. Such a layer should be clearly observable in [5, Figure 13]. Instead it seems as if the eroded projectile material has some remaining tensile strength or/and forward velocity so that it partly follows the residual projectile along the hole. Accordingly a significant part of the slower fragments in Figure 2 should come from the projectile, as also stated in [5, Figure 14]. If the total mass of fragments with mass 0+ g is assumed to be about equal to the groups with a few times larger mass, then the total mass of small projectile fragment should be about 110 g at the most. Accordingly the mass of projectile fragments that are deposited in the target could be up to about 220 g. This means that the *measured* target mass loss should be increased with this amount, so that the *significant fraction of target mass loss* should be even larger than the values above, namnely α≈0.93 and 0.90.

Exp.	530		607	
fragment	number of fragments		number of fragments	
mass, g	target	projectile	target	projectile
1.9+	1	0	1	0
1.8+	2	0	1	0
1.7+	0	0	0	0
1.6+	0	0	1	0
1.5+	1	0	1	0
1.4+	0	0	2	0
1.3+	0	0	2	0
1.2+	2	0	2	0
1.1+	3	5	0	5
1.0+	3	5	3	5
0.9+	3	10	0	10
0.8+	5	3	7	3
0.7+	5	5	2	10
0.6+	3	13	3	13
0.5+	3	13	2	17
0.4+	5	30	4	27
0.3+	11	37	2	43
0.2+	8	63	7	57
0.1+	26	?	14	110
0.0+	?	?	?	?
minimum sum, g	50.1	75.4	30.7	91.3
estimated sum, g	90	85	60	106
total mass loss, g	685	321.1	597	329.1

Table 1. Experimental results from [5, Figure 11]. Error in number of target fragments should be zero. Error in number of projectile fragments should be ±2 at the most.

Finally the validity of Eq. (6) for the total mass m_T of target fragments should be investigated. Since neither the mass m_1 of the largest fragment nor the number i of the largest fragment in Table 1 is known there is not sufficient information to determine the parameters B and λ. Accordingly one of these or i must be guessed. The average or representative values

m_T=(685+597)/2=641 g
m_i=1.9 g
$M(i)$-m_i=641-(60+90)/2=566 g
m_1=? (not known)
m_{i+11}=1.0 g
m_{i+29}=0.5 g

from Table 1 will be used. The three first relations yield

$$568 \approx 641\left\{1-\exp\left(-B\,i^{\lambda}\right)\right\}$$
$$1.9 \approx 641 B\,\lambda\, i^{\lambda-1}\exp\left(-B\,i^{\lambda}\right)$$

from which

$Bi^{\lambda}\approx 2.17$
$i\approx 84\lambda$

are obtained. Accordingly Eqs. (7), (6) and (10) yield

B=0.1
$i\approx 63$
$\lambda\approx 0.75$
$m_1\approx 61$ g
$m_{i+11}\approx 1.3$ g
$m_{i+29}\approx 0.8$ g

These calculated results for m_{i+11} and m_{i+29} are of the right magnitude but significantly larger than the values from Table 1. The calculated mass m_1 is about 10% of the total mass m_T, which might be a realistic result but intuitively seems to be too large.

Alternatively Eqs. (8), (6) and (10) yield

λ=0.5
$i\approx 42$
$B\approx 0.33$
$m_1\approx 180$ g
$m_{i+11}\approx 1.4$ g
$m_{i+29}\approx 0.8$ g

Here the calculated mass m_1 is even larger so this case seems less realistic than the former.

With an even smaller value B=0.05 one obtains

B=0.05
$i\approx 74$
$\lambda\approx 0.88$
$m_1\approx 31$ g
$m_{i+11}\approx 1.4$ g
$m_{i+29}\approx 0.7$ g

For $B<<1$ the case $\lambda>1$ yields $m_2>m_1$, which is not permitted for this model [6]. The limiting case corresponds to

λ=1
i≈84
B≈0.0258
m_1≈17 g
m_{i+11}=641{exp(-94B)-exp(-95B)}≈1.4 g
m_{i+29}=641{exp(-112B)-exp(-113B)}≈0.9 g

Accordingly a rather different model than that in Eq. (6) is required if significantly better agreement with the distribution in Table 1 shall be obtained. However, with regard to the differences between the two cases in Table 1, to the mixture of projectile and target fragments in Figure 2 and to other uncertainties the model is believed to be acceptable, at least at the present stage.

Discussion and conclusions

Projectile perforation of a thin target will perhaps produce a different distribution of fragment masses than that represented by Eqs. (6) – (8), for instance so that B is proportional to h/h^* whereas the value of λ is the same as for thick targets. However, new experimental results are required to estblish relations for B and λ for $h<h^*$.

The intended application of the model for projectile penetration, perforation and production of fragments, which is suggested in four previous papers and above, is in computer programs for assessment of effects and vulnerability of complex targets. Description of such targets and relevant warheads, in particular their interaction, requires that the phenomena must be modelled in rather simple ways. Continuum mechanics calculation for penetration and perforation is probably only possible in special cases. The suggested model, which covers rigid as well as eroding projectiles, is sufficiently compact for the intended application. If a fragment and/or its velocity is small enough, according to some appropriate rule, then this fragment should be neglected. Thus the infinite number of fragments corresponding to Eq. (5) is reduced to a finite number of fragments to be followed through a complex target. Besides the parameters B and λ, with the suggested values in Eqs. (6) and (7), a value for the mass fraction α in Eqs. (29) and (30) must be specified. At the present stage α=0.10 appears to be a reasonable choise, at least on the average.

High velocity fragments can certainly damage vital and vulnerable components in complex targets. Consequently they must be described as realistically as possible. This requires a realistic description of and close connection to the preceeding process, namely penetration and perforation. It is easily imagined that there is a region in front of the projectile that is crushed into much smaller fragments than those produced by spalling. Furthermore, the volume of such a region should be quite small compared to the volume of spalling fragments. Fragments in this small region should be directly accelerated by the residual projectile. Consequently they should have velocities that are comparable to the exit velocity of the projectile.

Spalling produces relatively large fragments for which the velocities are restricted to the particle velocities in elastic waves with stress amplitudes about equal to the yield strength of the material. For steel the upper velocity limit for spalling fragments is about 50 m/s. However, it is probable that some spalling fragments are accelerated to higher velocities when they are overtaken by the projectile and fragments from the faster-moving group.

With this general picture of target fragmentation during projectile perforation it is necessary to account for two different groups of target fragments. Due to the natural experimental scatter in fragment production a simpler procedure than that in Eqs. (16) - (19) and (22) should be sufficient for determination of directions of motion for the fragments. However, it is still necessary to let the fragments be ejected layer after layer,

as represented by Eqs. (10) - (15) and (20) - (21), in order to account for velocity reduction with increasing layer number in Eqs. (32) and (34).

The kinetic energy of a large and slowly moving (spalling) fragment is often many times smaller than that of a small but fast fragment. Nevertheless, the former can be important in the intended applications of the model. Quantification of vulnerability for vital components in complex targets is often based on incident energy rather than the combination of mass and velocity. Under such circumstances both fragment groups must be accounted for.

Presently the model is restricted to the simplest case of impact, namely along the normal direction to the impacted surface and with negligible projectile yaw.

References

1. G. Wijk, M. Hartmann, A. Tyrberg, A model for rigid projectile penetration and perforation of hard steel and metallic targets. FOI-R--1617--SE, April 2005.
2. G. Wijk, Initially increasing penetration resistance, friction and target size effects in connection with rigid projectile penetration of hard metallic targets. FOI-R--1631--SE, April 2005.
3. G. Wijk: Modell för eroderande projektilinträngning vid verkansvärdering (A model for eroding projectile penetration in vulnerabuility and lethality assessments). FOI-R--1446--SE, December 2004 (this report is a shortened and simplified version of the following reference).
4. G. Wijk, M. Hartmann, A. Tyrberg, A model for eroding projectile penetration and of metallic materials. Submitted for publication in *International Journal of Impact Engineering*.
5. A. L. Yarin, L. V. Roisman, K. Weber & V. Hohler, Model for ballistic fragmentation and behind-armor debris. *International Journal of Impact Engineering*, Vol. 24, pp. 171-201, 2000.
6. M. Held, Fragment mass distribution of “secondary fragments”. *Propellants, Expolsives, Pyrotechniques*, Vol. 16, pp. 21 - 26, 1991.
7. M. Hartmann, Behind-Armour Debris - Modelling and simulation. A literature review. FOI R --1678--SE, June 2005
8. I. Eriksson, Sekundärsplitter - Experimentella metoder. En litteraturstudie. FOI report to be released November-December 2005.
9. R. H. Cole, *Underwater explosions*. Princeton University Press, Princeton 1948.
10. D. E. Grady, The spall strength of condensed matter. *Journal of Mechanical Physics and Solids*, Vol. 36, No. 3, pp.353 - 384, 1988.
11. J. A. Zukas, *High Velocity Impact Dynamics*. John Wiley & Sons, New York (1990).

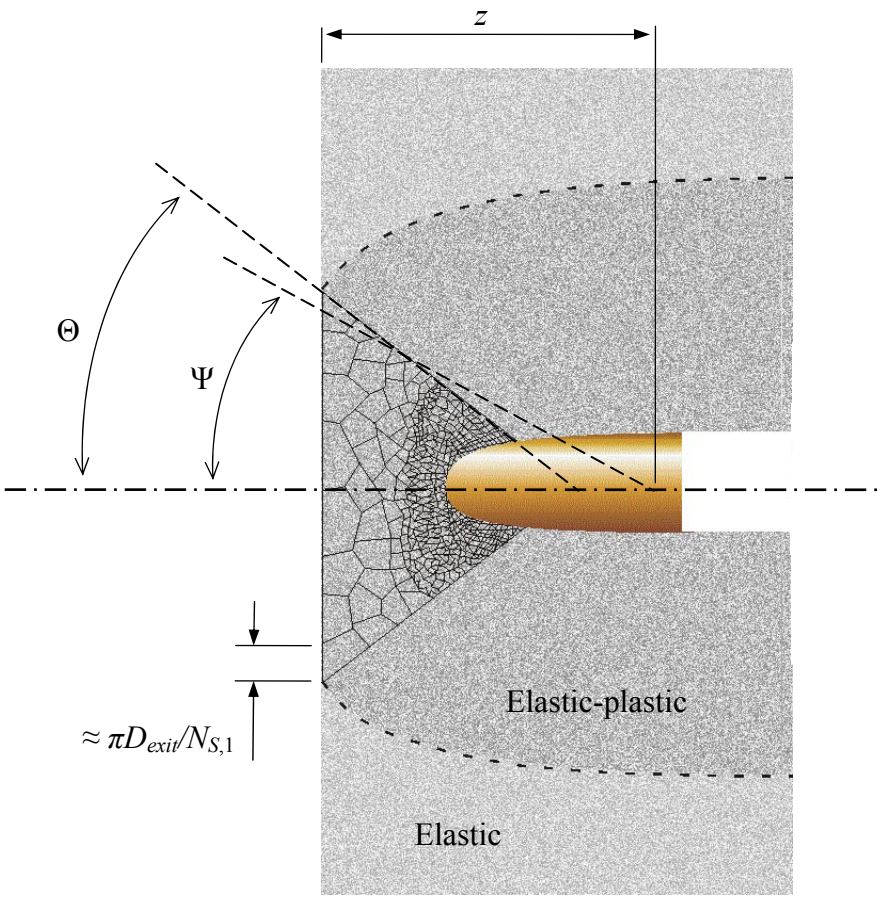

Figure 1. Schematic picture showing sudden production of fragments in front of a rigid projectile when the front end reaches the transition thickness h^* from the rear surface of the target. Previously the target material around the projectile and inside the broken line was subjected to elastic-plastic deformation, whereas the target material outside the broken line only was subjected to elastic deformation. In reality the elastic plastic boundary is 10 to 15 times larger than the projectile diameter d_P. The fragmented material in front of the projectile is located inside a conical surface with the half apex angle Θ and the diameter D_{exit} at the rear target surface. For clarity the angle Θ is exaggerated: in reality D_{exit} probably is a couple of times smaller than the elastic-plastic boundary diameter at the rear target surface. All fragments are approximated with cubes, the sizes of which decrease with increasing distance to the rear surface. The N_S surface fragments, which include the $N_{S,1}$ peripheral surface fragments, have the side length $\pi D_{exit}/N_{S,1}$. Extrapolations backwards of all fragment trajectories are assumed to join at a point along the axis at the distance z from the rear target surface. In reality the angle Θ may be smaller than the angle Ψ so that $z < h^*$.

In reality fragmentation is not instantaneous. Initially the larger surface fragments are detached due to elastic wave reflection, whereby the fragment velocities are restricted to the maximum particle velocity associated with such waves. Finally small fragments from the interior are accelerated through contact with the projectile and obtain velocities comparable to the exit velocity v_{exit} of the projectile. When v_{exit} is higher than the velocities produced via wave reflection there will be complicated interaction between the detached fragments. In the intended applications of the model such interaction must be neglected for reasons of simplicity. With this in mind the many other approximations and simplifications, which are necessary and consecutively suggested in the description of the model, become better justified. Moreover, some of these may even be considered to be unnecessarily ambitious.

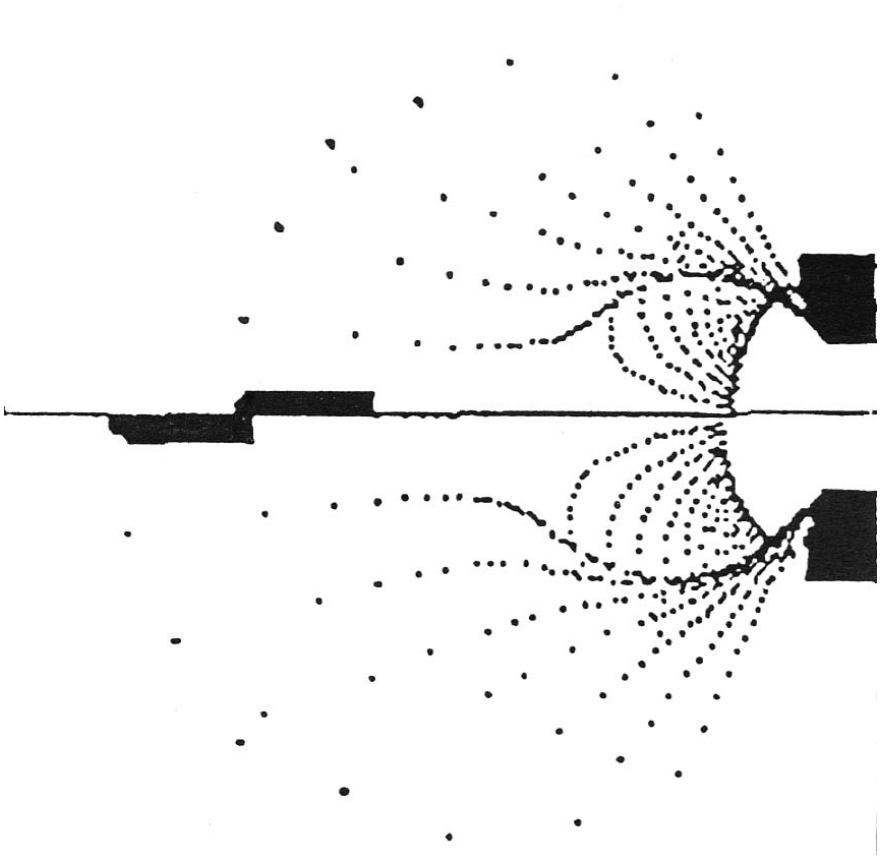

Figure 2. Calculated results in [5] for ejection of fragments from eroding projectile perforation of a target. The projectile diameter is d_P=20 mm. The initial external target diameter is slightly less than about twice the final hole diameter, which is much smaller than required in order to represent an infinitely wid target. After perforation the target diameter is increased with about 7% [5, Figure 13], which accounts for a significant part of volume of the hole through the target. The upper half of the figure is at time 200 μs and the lower half is at time 225 μs after impact of the initially flat-nosed projectile on the right target surface plane. The exit velocity of the residual projectile is v_{exit}≈1.6 km/s.

The calculations are carried out in axial symmetry (instead of full three-dimensionality). Thus every point corresponds to an "expanding" ring of fragments. Since all points are of equal size the figure does not describe the cross sectional areas but only the positions, velocities and directions of motion for the fragments in the rings. Moreover, since the projectile is eroding the fragments consist of both target and projectile material.

It is emphasized in [5] that the model does not account for all fragmented and ejected target material but only a minor fraction, typically about 10% or even less, which moves with velocities that are comparable to v_{exit}. The fragments in this minor fraction are (almost certainly) considerably smaller than the fragments in the remaining fraction, which previously must have been ejected via wave reflection at the rear target surface and, accordingly, move with initial velocities that are much smaller than v_{exit}.

Appendix: Perforation with eroding projectiles

Change from the penetration phase to the perforation phase in hard steel and metallic target material for blunt, rigid projectiles is modelled in [1]. The energy W_p required to perforate a target of thickness h without preceding penetration is a simple function of the target strength Y_T, the projectile diameter d_P and the thickness h

$$W_p = \frac{\pi}{8} h\, d_P \left(\pi h + 2 d_P\right) Y_T \,. \tag{A1}$$

When there is preceding penetration to the depth $P = h - h^*$, then the perforation energy is

$$W_p = \frac{\pi}{4} d_P^2 \left(h - h^*\right) \beta_T\, Y_T + W_p^*, \tag{A2}$$

where W_p^* is given by Eq. (1) with $h = h^*$. Thus W_p is a continuous function of h as it must be. The transition thickness h^* is determined by requiring that the derivative $\partial W_p / \partial h$ also is continuous, which yields

$$h^* = d_P \frac{\beta_T - 1}{\pi} \,. \tag{A3}$$

For eroding projectiles the following model for perforation is suggested. The first case to be considered is when the impact velocity is so great that the projectile always makes a hole which is larger than required for deposition of the instantaneously eroded projectile material. According to the model in [4] the hole depth at which the hole diameter becomes too small is given by $P_{\lim}$, which must be calculated with numerical integration. Thus the first case certainly occurs when $P_{\lim} > h$. When the penetration depth is $P = h - h^*$, whereby the velocity is v^* and hole diameter is D_T^*, the eroding projectile is assumed to become rigid and require the additional energy

$$W_p = \frac{\pi}{8} h^*\, D_T^* \left(\pi h^* + 2 D_T^*\right) Y_T \,. \tag{A4}$$

to accomplish perforation. The transition thickness h^* is determined by requiring that dw_T/du from [4, Eq. (5)] equals dW_p / dh^* from Eq. (A4), which yields

$$h^* = D_T^* \frac{\beta_T - 1}{\pi} = d_P \frac{v^* \left(\beta_T - 1\right)}{\pi\, v_T} \,. \tag{A5}$$

The model for eroding projectile penetration yields the instantaneous penetration depth $P(v)$ and projectile length $L(v)$ as functions of the instantaneous projectile velocity v. Accordingly Eq. (A5) and

$$P\left(v^*\right) = h - h^* \tag{A6}$$

must be solved numerically to yield the velocity v^*, and the cooresponding transition thickness h^*, at which penetration is changed to perforation. The corresponding hole diameter from [4, Eq. (2)] is

$$D_T^* = d_P \frac{v^*}{v_T}. \qquad \text{(A7)}$$

The total mass m_T of fragments that are ejected by the projectile when it leaves the target is

$$m_T = \frac{\pi}{4} D_T^{*2} h^* \rho_T. \qquad \text{(A8)}$$

The model represented by Eqs. (A5) – (A8) is not only valid for $P_{\text{lim}} > h$ but for $P_{\text{lim}} > h - h^*$. For $P_{\text{lim}} < h - h^*$ the projectile velocity and hole diameter decrease to v_{lim} and $D_{T,\text{lim}}$, respectively, at the penetration depth P_{lim}. The values v_{lim} and $D_{T,\text{lim}}$ are obtained from [4, Eqs. (15) and (17)]. For $P > P_{\text{lim}}$ the velocity continues to decrease and the hole diameter is constant. The transition thickness is given by

$$h^* = D_{T,\text{lim}} \frac{\beta_T - 1}{\pi}. \qquad \text{(A10)}$$

For $P_{\text{lim}} = h - h^*$ the corresponding velocity is v^* is equal to v_{lim} in [4, Eq. (17)].

It is not necessary to assume that the remainder of an eroding projectile becomes rigid when the penetration depth $P = h - h^*$ is reached. Erosion can be assumed to continue at some appropriate rate, for instance with dL/dP constant for $P \geq h - h^*$. Thereby additional energy is required for the corresponding deformation (shortening) of the projectile, as specified in [4], and should be added to W_p in Eqs. (A1) and (A2).